ADVANCED MATERIALS

Supporting Information

for *Adv. Mater.*, DOI: 10.1002/adma.201702712

Entropy as a Gene-Like Performance Indicator Promoting Thermoelectric Materials

Ruiheng Liu, Hongyi Chen, Kunpeng Zhao, Yuting Qin, Binbin Jiang, Tiansong Zhang, Gang Sha, Xun Shi, Ctirad Uher, Wenqing Zhang,* and Lidong Chen**

Supporting Information

Entropy as a gene-like performance indicator promoting thermoelectric materials

Ruiheng Liu†, Hongyi Chen†, Kunpeng Zhao, Yuting Qin, Binbin Jiang, Tiansong Zhang, Gang Sha, Xun Shi, Ctirad Uher, Wenqing Zhang*, Lidong Chen**

Experimental Section

Cu shot (99.999%, Alfa Aesar), Ag shot (99.999%, Alfa Aesar), S pieces (99.9999%, Alfa Aesar), Se shot (99.999%, Alfa Aesar), Ge pieces (99.999%, Alfa Aesar), Ga shot (99.9999%, Alfa Aesar), Mn, Sn, and Pb shots (99.999%, Alfa Aesar), Te shot (99.999%, Alfa Aesar). For $Cu_{2-z}Ag_zS_{1-x-y}Se_xTe_y$, the sealed tubes were slowly cooled to 650 °C from 1100 °C at a rate of 10 °C/h and then kept at 650 °C for 8 days. The obtained ingots were crushed into fine powders and followed by Spark Plasma Sintering (Sumitomo SPS 2040) under a pressure of 60 MPa at 600 °C for 20 min. For $Cu_{1-y}Ag_yIn_{1-x}Ga_xTe_2$, the silica tubes were quenched into ice cold water from 1100 °C and then annealed at 650 °C for 5 days. The obtained ingots were crushed into fine powders followed by hot press sintering (MRF Inc., USA) under a pressure of 65 MPa at 650 °C for 30 min. For $Mn_xGe_ySn_zPb_{1-x-y-z}Te$, the silica tubes were slowly cooled to 550 °C at a rate of 10 °C/h from 1000 °C and kept at 550 °C for 3 days. The obtained ingots were crushed into fine powders and followed by hot press sintering (MRF Inc., USA) under a pressure of 65 MPa at 550 °C for 30 min. For $(Cu_{1-y}Ag_y)_8Ge(Se_{1-x}Te_x)_6$, the silica tubes were quenched into ice cold water from 1100 °C and then annealed at 600 °C for 5 days. The obtained ingots were crushed into fine powders and followed by Spark Plasma Sintering (Sumitomo SPS 2040) under a pressure of 60 MPa at 550 °C for 20 min.

X-ray diffraction (XRD) analysis (Cu $K\alpha$, D8 ADVANCE, Bruker Co.Ltd) was employed to examine phase purity and crystal structures. Phase composition analysis at the micrometer scale was carried out by Electron Probe Microanalysis (EPMA, ZEISS Supra

55). APT was performed at 20 K in a CAMECA instrument (LEAP 4000X Si) by applying ultraviolet laser pulsing with a wavelength of 355 nm, an energy of 10 pJ, a pulse repetition rate of 200 kHz, and a target ion collection rate of 5%. We used CAMECA IVAS 3.6.8 software to analyze the data. Samples in the form of sharp needles for APT analysis were prepared by a focused ion beam lift-off methodology (Zeiss Augraga FIB/SEM) by using Ga ion beam milling. High-temperature Seebeck coefficient (α) and electrical conductivity (σ) were measured using a ZEM-3 instrument (ULVAC Co. Ltd.) under a sealed chamber with a small amount of helium gas. The thermal diffusivity (λ) and heat capacity (C_P) from 300 K to 1000 K were measured using the laser flash method (Netzsch, LFA427) and differential scanning calorimetry (Netzsch DSC 404F3), respectively. The density (d) was measured using the Archimedes method. The thermal conductivity was calculated from $\kappa = \lambda \times C_P \times d$. Room temperature Hall coefficient (R_H) measurements were performed using Quantum Design PPMS by sweeping the magnetic field up to 3 T in both positive and negative directions. The hole concentration (p) is calculated from $p = 1/qR_H$, where q is the elementary charge.

For a binary solution reaction

$$(1-x)AB + xA'B \rightarrow A_{1-x}A'_xB, \quad \text{S1}$$

the change in enthalpy $\Delta H_{A_{1-x}A'_xB}$ is

$$\Delta H_{A_{1-x}A'_xB} = H_{A_{1-x}A'_xB} - (1-x)H_{AB} - xH_{A'B} = x\int_1^x \Delta H_{cell} \cdot \frac{N_A}{Z} dt + (1-x)\int_0^x \Delta H_{cell} \cdot \frac{N_A}{Z} dt, \quad \text{S2}$$

where N_A is the Avogadro's number, and $\Delta H_{cell}(t)$ is the enthalpy change due to one $A'B$ unit cell replacing one AB unit cell in $A_{1-t}A'_tB$. $\Delta H_{cell}(t)$ has two components, the internal strain energy $\Delta H^S_{cell}(t)$ caused by the atomic size mismatch and the internal ionic field energy $\Delta H^C_{cell}(t)$ caused by electron cloud redistribution.

Assuming $A_{1-t}A'_tB$ is an elastic continuous sphere with a vacancy of one unit cell, the internal strain energies by inserting $A'B$ ($\Delta H^S_{A'B}(t)$) or AB ($\Delta H^S_{AB}(t)$) unit cells into the vacancy are calculated by using the elastic deformation equation[1,2]

$$\Delta H^S_{A'B}(t) = \int_0^\infty \frac{1}{2}\vec{\varepsilon}\vec{\delta} 4\pi r^2 dr = 8\pi G_{AA'} R_{AA'}{}^3 \chi^2_{A'} c_{A'}, \quad \text{S3}$$

where $\chi_{A'} = \frac{R_{A'}-R_{AA'}}{R_{AA'}}$, $c_{A'} = \frac{3K_{A'}}{4G_{AA'}+3K_{A'}}$, $K_{A'}$ is the bulk modulus of $A'B$, $R_{AA'}(t)$ and $G_{AA'}(t)$ are the circumradius and shear modulus of the matrix $A_{1-t}A'_t$B, respectively, which can be regarded as the linear combination of AB and $A'B$. Assuming there are tN $A'B$ unit cells dispersed in a spherical matrix with a cut-off radius $\acute{R}$, by adding the extra increased internal energy by the first-order effect of surface tension, $\Delta H^S_{A'B}(t)$ becomes[3,4]

$$\Delta H^S_{A'B}(t) = 8\pi G_{AA'}{R_{AA'}}^3 \chi^2_{A'} c_{A'}(1-2t). \quad \text{S4}$$

$\Delta H^S_{AB}(t)$ is obtained by the same approach. Then,

$$\Delta H^S_{cell}(t) = \Delta H^S_{A'B}(t) - \Delta H^S_{AB}(t) = 8\pi G_{AA'}{R_{AA'}}^3 \chi^2_{A'} c_{A'}(1-2t) - 8\pi G_{AA'}{R_{AA'}}^3 \chi^2_{A} c_{A}(2t-1), \quad \text{S5}$$

The total increased internal strain energy ($\Delta H_S(x)$) is

$$\Delta H_S(x) = x\int_1^x \frac{\Delta H^S_{cell}(t)}{Z}\cdot N_A\,dt + (1-x)\int_0^x \frac{\Delta H^S_{cell}(t)}{Z}\cdot N_A\,dt$$
$$\approx 8\pi\frac{N_A}{Z}G_A R_A(R_A-R_{A'})^2\frac{3K_{A'}}{4G_A+3K_{A'}}f_0 - 8\pi\frac{N_A}{Z}G_{A'}R_{A'}(R_A-R_{A'})^2\frac{3K_A}{4G_{A'}+3K_A}f_1, \quad \text{S6}$$

where $f_0 = x\int_1^x(1-t)^2(2t-1)dt + (1-x)\int_0^x(1-t)^2(2t-1)dt$, and $f_1 = x\int_1^x t^2(1-2t)dt + (1-x)\int_0^x t^2(1-2t)dt$.

When x = 0.5, ΔH_S achieves its maximum value, and then $f_0 = -f_1 \approx 0.09375$. Furthermore, in semiconductors, G/K is about 0.5[5], and $\Delta H_S(x)$ is then well-fitted by the 2nd-degree Taylor polynomial at x = 0.5,

$$\Delta H_S(x) \approx MN_A\cdot[\bar{G}\,\overline{R^*}(\Delta R^*)^2/Z]\cdot(1-x)x = MN_A\cdot\delta\cdot(1-x)x, \quad \text{S7}$$

where δ is the solubility parameter (defined by $\delta = \bar{G}\,\overline{R^*}(\Delta R^*)^2/Z$), R^* is the effective lattice constant (defined by $R^* = \sqrt{\frac{a^2+b^2+c^2}{3}}$ for an orthorhombic structure and $\sqrt{\frac{(2a)^2+c^2}{3}}$ for a hexagonal structure, where a, b and c are the parameters of a unit cell, or the parameters of a supercell that is built close to a sphere), $\bar{G}$ and $\overline{R^*}$ are the average shear modulus and the effective lattice constant of AB and $A'B$, ΔR^* is the difference in effective lattice constants between AB and $A'B$ ($\Delta R^* = |{R^*}_{AB} - {R^*}_{A'B}|$), $M = \frac{72\sqrt{3}\pi\times 0.09375}{4G/K+3} \approx 7.34$.

A ternary solution $(A_{1-x}A'_x)_{1-y}A''_yB$ can be divided into three binary solutions

$$(1-y)AB + (1-y)A''B \rightarrow A_{1-y}A''_yB\,, \quad \text{S8-1}$$

$$(1-y)A'B + (1-y)A''B \rightarrow A'_{1-y}A''_yB, \quad \text{S8-2}$$

$$(1-x)A_{1-y}A''_yB + xA'_{1-y}A''_yB \rightarrow (A_{1-x}A'_x)_{1-y}A''_yB, \quad \text{S8-3}$$

The change in the internal strain energy of the first two binary solutions $\Delta H_1(y)$, $\Delta H_2(y)$ can be calculated according to Equation S7. For the third quasi-binary solution, $\Delta H_3(x,y)$ is

$$\Delta H_3(x,y) \approx 8\pi \frac{N_A}{Z} G_A' R_A' (R_A' - R_{A'}')^2 \frac{3K_{A'}'}{4G_A' + 3K_{A'}'} f_0 - 8\pi \frac{N_A}{Z} G_{A'}' R_{A'}' (R_A' - R_{A'}')^2 \frac{3K_A'}{4G_{A'}' + 3K_A'} f_1, \quad \text{S9}$$

where $R_A', R_{A'}', R_{AA'}', K_A', K_{A'}', G_A', G_{A'}'$, have the same definitions as those in binary systems. However, Equation S9 neglects the internal stress and strain caused by the first-order effect of surface tension of the $A''B$ unit cell, which has to be considered and added. Then, f_0 and f_1 in Equation S9 are modified as

$$f_0 = x\int_1^x (1-t)^2 \left(2t - 1 - 2\frac{R_{A''} - R_{AA'}'}{R_A' - R_{AA'}'} y\right) dt + (1-x)\int_0^x (1-t)^2 \left(2t - 1 - 2\frac{R_{A''} - R_{AA'}'}{R_A' - R_{AA'}'} y\right) dt \quad \text{and}$$

$$f_1 = x\int_1^x t^2 \left(1 - 2t - 2\frac{R_{A''} - R_{AA'}'}{R_{A'}' - R_{AA'}'} y\right) dt + (1-x)\int_0^x t^2 \left(1 - 2t - 2\frac{R_{A''} - R_{AA'}'}{R_{A'}' - R_{AA'}'} y\right) dt.$$

To simplify $\Delta H_3(x,y)$, it can be written as a product of two terms

$$\Delta H_3(x,y) \approx \Delta H_3(x,0) \cdot f\left(y, \frac{R_{A''}}{R_{AA'}}\right). \quad \text{S10}$$

where $\Delta H_3(x,0)$ is the internal strain energy for a binary solution $A_{1-x}A'_xB$, and $f\left(y, \frac{R_{A''}}{R_{AA'}}\right)$ is a function representing the effect of an extra component $A''B$. As shown in Figure S2, the $f\left(y, \frac{R_{A''}}{R_{AA'}}\right)$ can be well fit by (1-y)$^{3.5}$ when $\frac{R_{A''}}{R_{AA'}}$ varies from 80% ~ 120%. Thus,

$$\Delta H_3(x,y) \approx MN_A \cdot \delta_{AA'} \cdot (1-x)x \cdot (1-y)^{3.5}, \quad \text{S11}$$

where $\delta_{AA'}$ is the solubility parameter of a binary solution $A_{1-x}A'_xB$.

Consequently, the calculated total internal strain energy of the ternary solution in Equation S8 is

$$\Delta H_{\text{total}} = x\Delta H_1(y) + (1-x)\Delta H_2(y) + \Delta H_3(x,y), \quad \text{S12}$$

Considering all the different solution routes, the average ΔH_{total} for achieving an equimolar ternary solution is

$$\Delta \bar{H}_{\text{total}} = MN_A \cdot \bar{\delta} \cdot \left[\sum_{i=2}^{3} \left(1 - \frac{1}{i}\right) \frac{1}{i} \cdot \left(\frac{i}{3}\right)^{3.5}\right], \quad \text{S13}$$

where $\bar{\delta}$ is the average δ value of all separate binary solutions.

Using the same approach, for a multi-component material $(A_{1-x}A'_x)_{1-y1-y2\ldots}A''_{y1}A'''_{y2}\ldots B$, $\Delta H_S(x, y1, y2\ldots)$ we write

$$\Delta H_S(x, y1, y2\ldots) \approx MN_A \cdot \delta_{AA'} \cdot (1-x)x \cdot (1-y_{total})^{3.5}, \quad \text{S14}$$

where $y_{total} = \text{y1} + \text{y2} + \cdots$. For equimolar multi-component solutions, $\Delta \bar{H}_{\text{total}}$ is given by

$$\Delta \bar{H}_{total} = MN_A \cdot \bar{\delta} \cdot \left[\sum_{i=2}^{n} \left(1 - \frac{1}{i}\right) \frac{1}{i} \cdot \left(\frac{i}{n}\right)^{3.5}\right]. \quad \text{S15}$$

For the change in the internal ionic field energy $\Delta H_{cell}^{c}(t)$, the effective charge (Q) of A (or A') in AB (or $A'B$) is estimated and calculated based on the developed Pauling electronegativity[6]. For $A_{1-t}A'_tB$, the average effective charge of A (A') atomic positions can be assumed to be a linear combination of Q_A and $Q_{A'}$. Then, according to the Born–Landé equation[7], $\Delta H_{cell}^{c}(t)$ is

$$\Delta H_{cell}^{c}(t) = -\frac{M_A \cdot Q_{AA'} \cdot (Q_A - Q_{A'})}{4\pi\varepsilon_0 R_{AA'}} - \frac{M_B \cdot Q_B \cdot (Q_A - Q_{A'})}{4\pi\varepsilon_0 R_{AA'}}, \quad \text{S16}$$

where ε_0 is the vacuum permittivity, and M_A and M_D are the Madelung constants for atom A (A') and B. $\Delta H_c(x)$ then becomes

$$\Delta H_c(x) = x\int_1^x -\Delta H_{cell}^{c}(t) \cdot N_A\, dt + (1-x)\int_0^x -\Delta H_{cell}^{c}(t) \cdot N_A\, dt. \quad \text{S17}$$

The calculated ΔH_S and ΔH_c for several TE materials are listed in Table S1.

Figures S1 to S9.

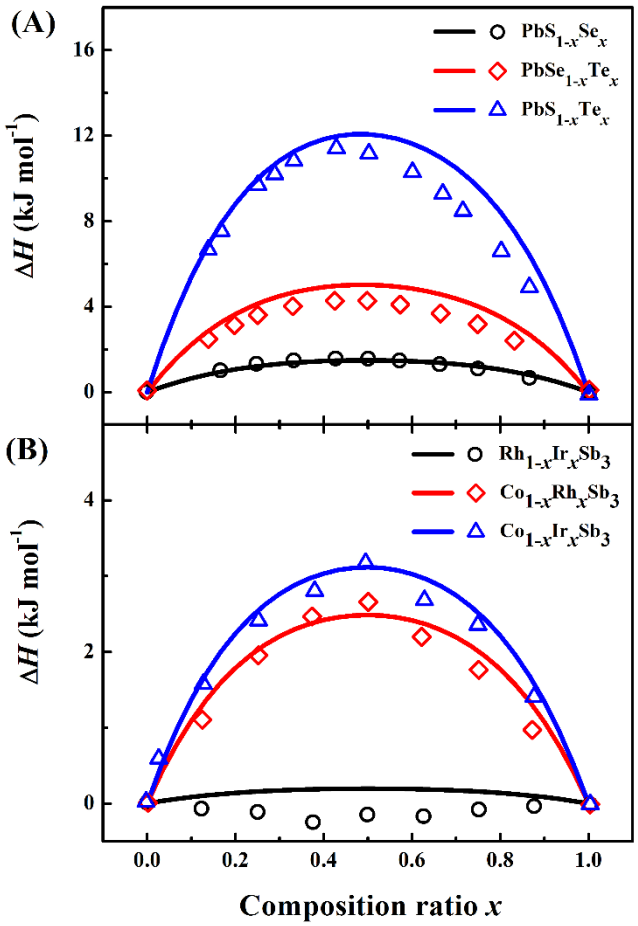

Figure S1. Calculated changes in enthalpy (ΔH) based on Equation S6 for several two-component TE materials. The lines are calculated according to our model. The dots are calculated by *ab initio* calculations taken from Supporting Ref. 8 and 9.

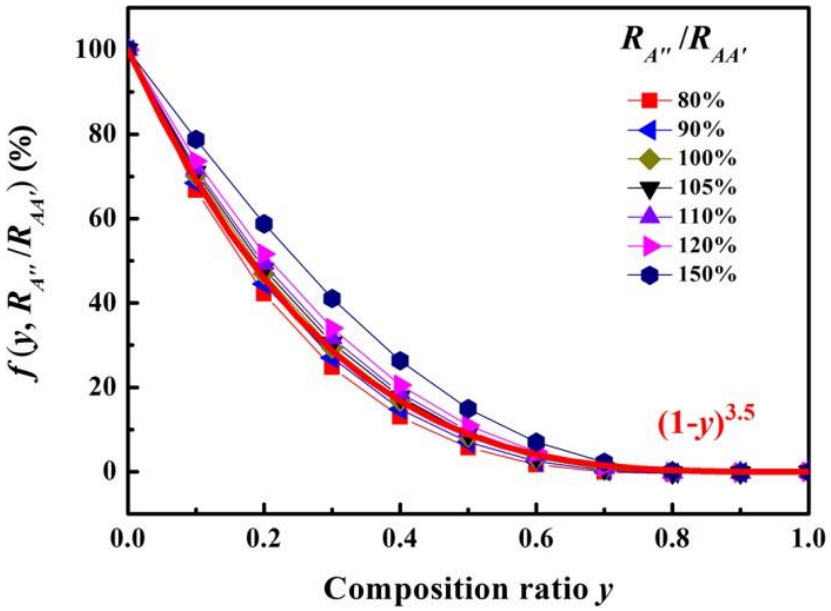

Figure S2. Function $f\left(y, \frac{R_{A''}}{R_{AA'}}\right)$ depending on y and $\frac{R_{A''}}{R_{AA'}}$. Curves marked with symbols are calculated according to Equation S9, and the red curve is the fitting result represented by $(1-y)^{3.5}$.

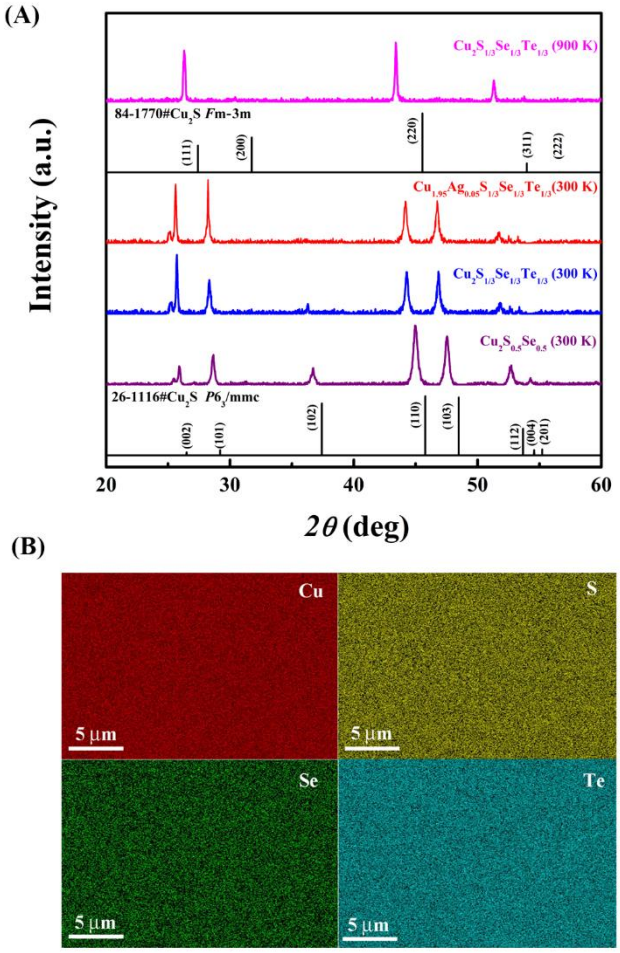

Figure S3. (A) Powder X-ray diffraction patterns of $Cu_2S_{0.5}Se_{0.5}$, $Cu_2S_{1/3}Se_{1/3}Te_{1/3}$, and $Cu_{1.95}Ag_{0.05}S_{1/3}Se_{1/3}Te_{1/3}$. They exhibit a hexagonal structure with the space group of $P6_3/mmc$ at 300 K. The uppermost trace shows a cubic structure of $Cu_2S_{1/3}Se_{1/3}Te_{1/3}$ with the space group of $Fm\text{-}3m$ at 900 K. (B) Elemental maps of $Cu_2S_{1/3}Se_{1/3}Te_{1/3}$ obtained by Electron Probe Microanalysis (EPMA).

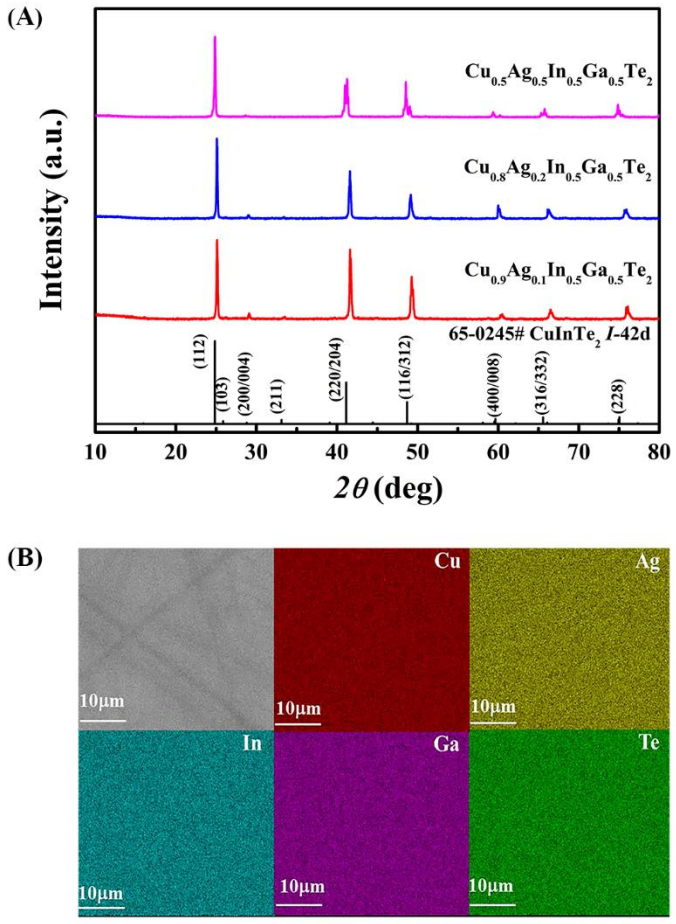

Figure S4. (A) Powder X-ray diffraction patterns of a series of (Cu/Ag)(In/Ga)Te_2-based multi-component TE materials. (B) Elemental maps of $Cu_{0.5}Ag_{0.5}In_{0.5}Ga_{0.5}Te_2$ obtained by Electron Probe Microanalysis (EPMA).

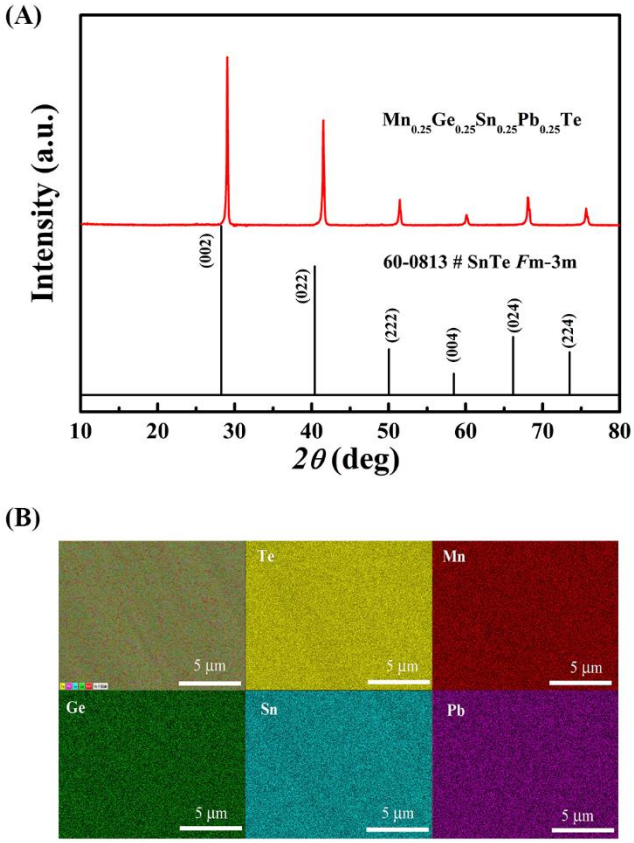

Figure S5. (A) Powder X-ray diffraction pattern of $Mn_{0.25}Ge_{0.25}Sn_{0.25}Pb_{0.25}Te$. (B) Elemental maps of $Mn_{0.25}Ge_{0.25}Sn_{0.25}Pb_{0.25}Te$ obtained by Electron Probe Microanalysis (EPMA).

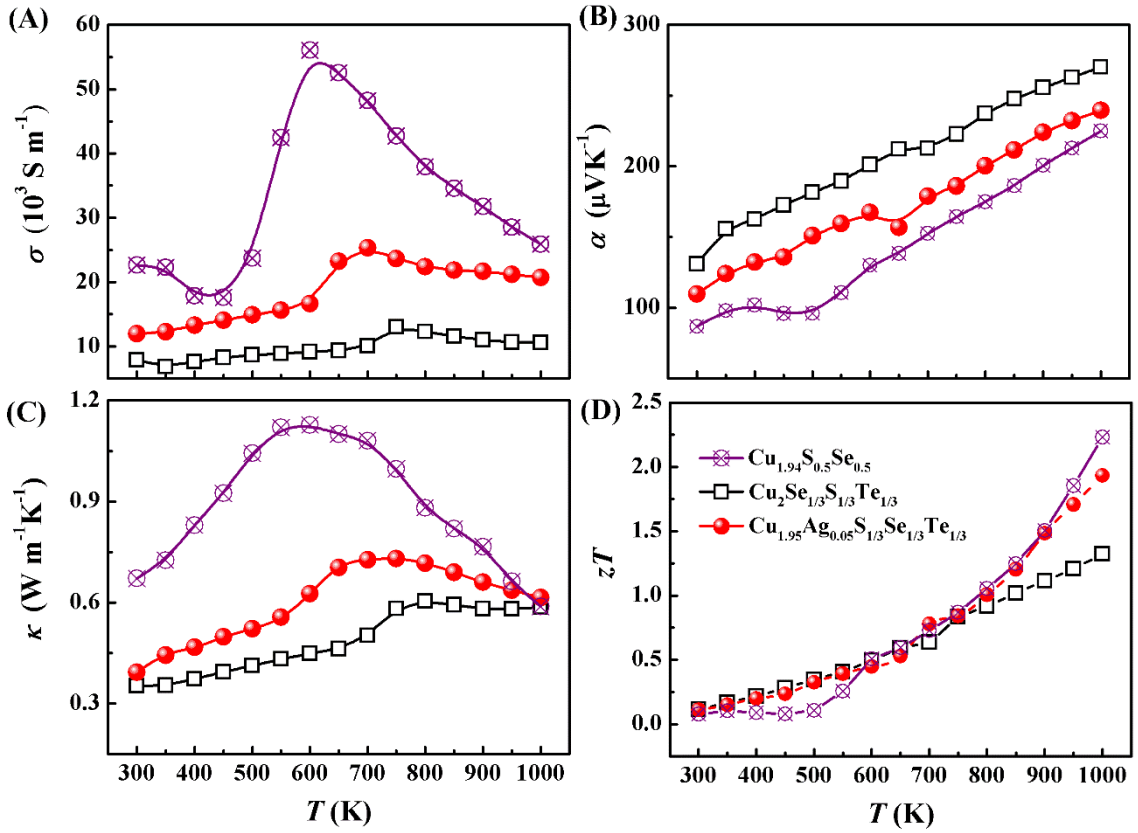

Figure S6. Temperature dependence of the electrical conductivity (A), Seebeck coefficient (B), thermal conductivity (C) and the thermoelectric figure of merit (*zT*) (D) for Cu_2(S/Se/Te)-based multi-component TE materials.

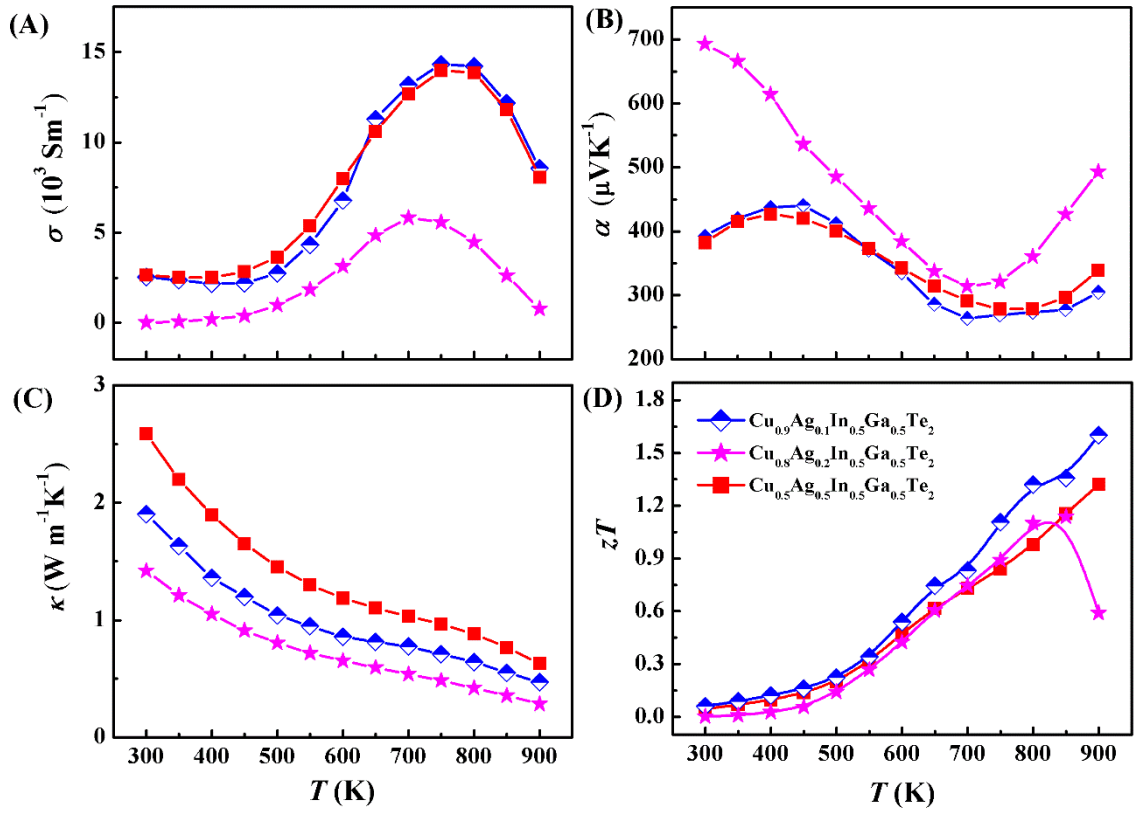

Figure S7. Temperature dependence of the electrical conductivity (A), Seebeck coefficient (B), thermal conductivity (C) and the figure of merit (zT) (D) for (Cu/Ag)(In/Ga)Te_2-based multi-component TE materials.

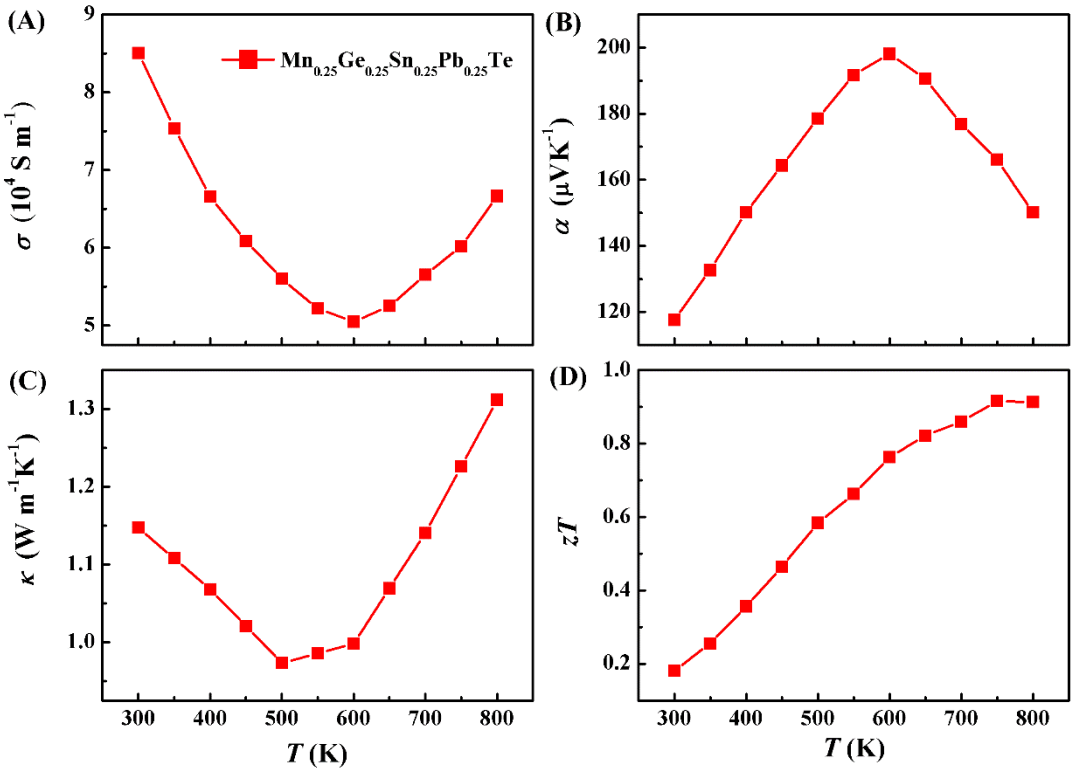

Figure S8. Temperature dependence of the electrical conductivity (A), Seebeck coefficient (B), thermal conductivity (C) and the figure of merit (zT) (D) for $Mn_{0.25}Ge_{0.25}Sn_{0.25}Pb_{0.25}Te$ multi-component TE materials.

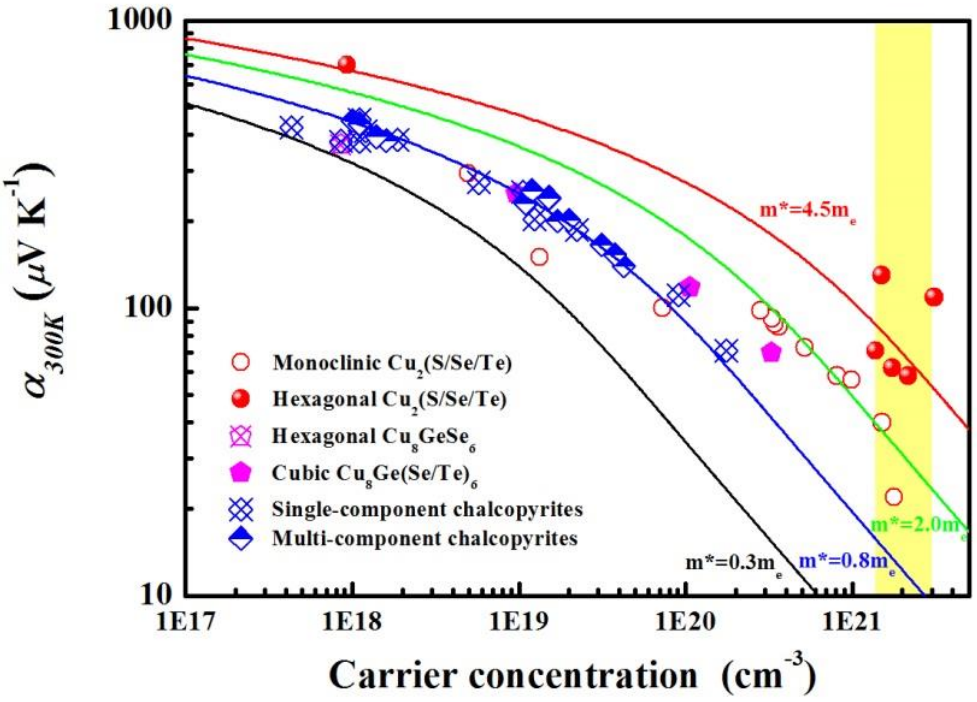

Figure S9. Hall carrier concentration dependence of room temperature Seebeck coefficient of Cu_2(S/Se/Te)-, (Cu/Ag)(In/Ga)Te_2-, and $Cu_8Ge(Se/Te)_6$-based TE materials. The effective mass is estimated from the single parabolic band model.

Tables S1 to S4.

Table S1. Internal strain energy (ΔH_S) arising from the atomic size mismatch, fluctuation of the internal ionic field energy (ΔH_C) from electron cloud redistribution, $\Delta H_C/\Delta H_S$, and the formation enthalpy (ΔH) for various binary TE solutions with equal atomic-ratio components.

Systems	ΔH_C [J mol^{-1}]	ΔH_C [k_BT/f.u.]	ΔH_S [J mol^{-1}]	$\Delta H_C/\Delta H_S$	ΔH [J/mol]
PbSe-PbTe	316.7	0.13	5025.8	6.30%	5342.5
PbS-PbTe	40.3	0.02	12069.6	0.33%	12109.9
PbS-PbSe	-38.9	-0.02	1499.1	-2.59%	1460.2
$CoSb_3$-$IrSb_3$	440.5	0.18	3116.8	14.13%	3557.3
$CoSb_3$-$RhSb_3$	916.5	0.37	2487.0	36.85%	3403.5
$CuInTe_2$-$AgInTe_2$	13.8	<0.01	276.9	4.98%	290.7

Table S2. Space group, number of components (*n*), average shear modulus ($\bar{G}$), average effective lattice constant ($\overline{R^*}$), and parameter $\bar{\delta}$ for various systems of multi-component TE materials.

NO.	Systems	Space group	*n*	$\bar{G}$ [GPa]	$\overline{R^*}$ [Å]	$\bar{\delta}$ [GPa·Å^3]
1	TiCoSb-ZrCoSb-HfCoSb	*F*m-3m	3	76	6.01	1.85
2	$CoSb_3$-$RhSb_3$-$IrSb_3$	*I*m-3	3	63	9.18	2.14
3	Cu_2S-Cu_2Se-Cu_2Te	(LT) *P*2$_1$/c, *C*2/c; (MT) *P*6$_3$/mmc; (HT) *F*m-3m	3	26	5.91	2.39
4	ZnTe-CdTe-HgTe	*F*-43m	3	16	6.35	2.40
5	TiNiSn-ZrNiSn-HfNiSn	*F*-43m	3	90	6.04	2.45
6	$CuGaTe_2$-$CuInTe_2$ -$AgGaTe_2$-$AgInTe_2$	*I*-42d	4	22	8.71	3.12
7	MnTe-GeTe-SnTe-PbTe	*F*m-3m	4	19	6.18	3.36
8	PbS-PbSe-PbTe	*F*m-3m	3	27	6.19	4.57
9	AlSb-GaSb-InSb	*F*-43m	3	53	6.25	7.01

Table S3. Seebeck coefficient (α), electrical conductivity (σ), thermal conductivity (κ), carrier concentration (p) at 300 K, and the maximum TE figure of merit at corresponded temperatures ($(zT)_{max}$) of various single component and multi-component TE materials.

Compositions	α [μV K^{-1}]	σ [S m^{-1}]	κ [Wm^{-1}K^{-1}]	P [cm^{-3}]	$(zT)_{max}$
$Cu_{1.92}S$[10]	40	4.10×10^{4}	1.06	2.50×10^{21}	0.57
$Cu_{1.9}Se$	40	3.48×10^{5}	2.16	1.51×10^{21}	0.43
Cu_2Te[11]	25	4.10×10^{5}	2.08	1.78×10^{21}	0.56
$Cu_2Se_{0.8}Te_{0.2}$	44	1.32×10^{5}	1.37	1.10×10^{21}	0.80
$Cu_2Se_{0.5}Te_{0.5}$	40	1.20×10^{5}	1.03	1.12×10^{21}	1.11
$Cu_2S_{0.50}Te_{0.50}$[12]	58	3.13×10^{4}	0.52	2.17×10^{21}	2.10
$Cu_2S_{0.52}Te_{0.48}$[12]	62	2.77×10^{4}	0.48	1.74×10^{21}	1.83
$Cu_2S_{0.54}Te_{0.46}$[12]	71	1.92×10^{4}	0.41	1.37×10^{21}	1.70
$Cu_{1.94}S_{0.5}Se_{0.5}$	87	2.27×10^{4}	0.67	1.34×10^{21}	2.23
$Cu_2S_{1/3}Se_{1/3}Te_{1/3}$	130	7.87×10^{3}	0.35	1.50×10^{21}	1.32
$Cu_{1.95}Ag_{0.05}S_{1/3}Se_{1/3}Te_{1/3}$	109	1.19×10^{4}	0.39	3.01×10^{21}	1.92
$CuInTe_2$[13]	204	9.70×10^{3}	6.03	1.24×10^{19}	1.02
$Cu_{0.99}GaTe_2$[14]	263	1.59×10^{4}	7.80	1.22×10^{19}	0.70
$Cu_{0.99}In_{0.5}Ga_{0.5}Te_2$[14]	202	2.54×10^{4}	3.50	1.59×10^{19}	0.82
$Cu_{0.88}Ag_{0.1}InTe_2$[15]	201	1.35×10^{4}	2.84	1.70×10^{19}	1.09
$Cu_{0.75}Ag_{0.2}InTe_2$[15]	231	7.10×10^{3}	1.84	1.11×10^{19}	1.24
$Cu_{0.88}Ag_{0.1}InTe_2$[15]	211	1.42×10^{4}	2.90	2.00×10^{19}	0.68
$Cu_{0.75}Ag_{0.2}InTe_2$[15]	242	8.20×10^{3}	1.95	1.52×10^{19}	0.77
$Cu_{0.9}Ag_{0.1}In_{0.5}Ga_{0.5}Te_2$	382	2.63×10^{3}	2.58	1.75×10^{18}	1.32
$Cu_{0.8}Ag_{0.2}In_{0.5}Ga_{0.5}Te_2$	392	2.55×10^{3}	1.90	1.90×10^{18}	1.60
$Cu_{0.5}Ag_{0.5}In_{0.5}Ga_{0.5}Te_2$	693	2.54×10^{1}	1.42	-	1.13
$Mn_{0.25}Ge_{0.25}Sn_{0.25}Pb_{0.25}Te$	118	4.98×10^{4}	1.15	-	0.91
Cu_8GeSe_6	235	3.23×10^{0}	0.31	8.48×10^{17}	0.54
$Cu_8GeSe_{5.7}Te_{0.3}$	284	1.52×10^{2}	0.29	9.56×10^{18}	0.71
$Cu_8GeSe_{5.4}Te_{0.6}$	104	1.35×10^{4}	0.51	1.06×10^{20}	0.89
$Cu_{7.6}Ag_{0.4}GeSe_{5.1}Te_{0.9}$	88	3.57×10^{4}	0.41	4.38×10^{20}	1.07

Table S4. Space group, shear modulus (G), lattice parameters (a and c), unit cell volume (V_{cell}), number of formula units (Z) in one unit cell for typical TE materials.

Compounds	Space group	G [GPa]	Lattice parameter		V_{cell} [Å^3]	Z
			a [Å]	c [Å]		
PbS	*F*m-3m	30	5.996	-	215	4
PbSe	*F*m-3m	27	6.140	-	231	4
PbTe	*F*m-3m	23	6.440	-	268	4
Bi_2Te_3[a)]	*R*-3m	52	4.390	30.480	-	3
Sb_2Te_3[a)]	*R*-3m	-	4.260	30.400	-	3
Bi_2Se_3[a)]	*R*-3m	-	4.130	28.600	-	3
SnTe	*F*m-3m	10	6.310	-	251	4
GeTe	*F*m-3m	25	5.985	-	214	4
MnTe	*F*m-3m	-	5.980		214	4
$CoSb_3$	*I*m-3	56	9.034	-	737	8
$RhSb_3$	*I*m-3	63	9.242	-	786	8
$IrSb_3$	*I*m-3	70	9.253	-	792	8
$CuInTe_2$	*I*-42d	19	6.194	12.416	476	4
$AgInTe_2$	*I*-42d	14	6.401	12.613	515	4
$CuGaTe_2$	*I*-42d	26	6.024	11.929	432	4
$AgGaTe_2$	*I*-42d	28	6.296	11.990	475	4
ZnTe	*F*-43m	20	6.104	-	227	4
CdTe	*F*-43m	18.3	6.481	-	272	4
HgTe	*F*-43m	8.9	6.461	-	270	4
Cu_2S	(HT) *F*m-3m[b)]	17.8[c)]	5.762	-	191	4
Cu_2Se	(HT) *F*m-3m[b)]	36.3[c)]	5.871	-	202	4
Cu_2Te	(HT) *F*m-3m[b)]	25[c)]	6.114	-	228	4
AlSb	*F*-43m	58	6.135	-	231	4
GaSb	*F*-43m	56	6.118	-	229	4
InSb	*F*-43m	46	6.487	-	273	4
TiNiSn	*F*m-3m	76	5.921	-	208	4
ZrNiSn	*F*m-3m	-	6.113	-	228	4
HfNiSn	*F*m-3m	-	6.084	-	225	4
TiCoSb	*F*m-3m	90.5	5.913	-	207	4
ZrCoSb	*F*m-3m	-	6.068	-	223	4
HfCoSb	*F*m-3m	-	6.040	-	220	4

$SrZn_2Sb_2$	*P*-3m1	-	4.500	7.716	135	1
$CaZn_2Sb_2$	*P*-3m1	-	4.441	7.464	127	1
$EuZn_2Sb_2$	*P*-3m1	25	4.480	7.601	133	1
$YbZn_2Sb_2$	*P*-3m1	-	4.446	7.426	127	1

[a] For Bi_2Te_3-based materials, a supercell with lattice parameters of ($4a^*\times4b^*\times c^*$) is used, where a^*, b^*, and c^* are the lattice parameters of a conversional unit cell;

[b] The lattice parameters of high temperature cubic structure are used [16,17] ;

[c] Shear modulus is calculated based on the reported acoustic velocity[11,18].

Supporting References:

[1] D. Feng, D. R. Qiu, *Physics in metals: Structure and Defects*, Beijing: Science press, **1998**, p. 172.

[2] J. D. Eshelby, *Solid State Phys.* **1956**, *3*, 79.

[3] H. Sonomura, *J. Appl. Phys.* **1986**, *59(3)*, 739.

[4] W. S. Slaughter, *The linearized theory of elasticity*, Birkhauser, Boston, **2002**, p. 193.

[5] G. N. Greaves, A. L. Greer, R. S. Lakes, T. Rouxel, *Nat. Mater.* **2011**, *10*, 823.

[6] J. C. Phillips, *Rev. Mod. Phys.* **1970**, *42(3)*, 317.

[7] I. D. Brown, *The chemical bond in inorganic chemistry: the bond valence model* (Reprint. ed.), Oxford University Press, Oxford, **2002**.

[8] J. W. Doak, C. Wolverton, *Phys. Rev. B* **2012**, *86*, 144202.

[9] X. Shi, Z. Zhou, W. Zhang, L. D. Chen, J. Yang, C. Uher, *J. Appl. Phys.* **2007**, *101(12)*, 123525.

[10] P. F. Qiu, Y.Q. Zhu, Y.T. Qin, X. Shi, L. D. Chen, *APL Mater.* **2016**, *4*, 104805.

[11] Y. He, T. S. Zhang, X. Shi, S. H. Wei, L. D. Chen, *NPG Asia Mater.* **2015**, *7*, e210.

[12] Y. He, P. Lu, X. Shi, F.F. Xu, T. S. Zhang, G. J. Snyder, C. Uher, L. D. Chen, *Adv. Mater.* **2015**, *27(24)*, 3639.

[13] N. Cheng, R. H. Liu, S. Q. Bai, X. Shi, L. D. Chen, *J. Appl. Phys.* **2014**,*115*, 163705.

[14] Y. T. Qin, P. F. Qiu, R. H. Liu, Y. L. Li, F. Hao, T. S. Zhang, D.D. Ren, X. Shi, L. D. Chen, *J. Mater. Chem. A* **2016**, *4*, 1277.

[15] R. H. Liu, Y. T. Qin, N. Cheng, J. W. Zhang, X. Shi, Y. Grin, L. D. Chen, *Inorg. Chem. Front.* **2016**, *3*,1167.

[16] M. Oliveria, R. K. Mcmullan, B. J. Wuensch, *Solid State Ionics* **1988**, *28*, 1332.

[17] Y. G. Asadov, S. Y. Asadova, A. Movlamverdieva, F. K. Isaev, *Inor. Mater.* **2002**, *38*,1103.

[18] Y. He, T. Day, T. S. Zhang, X. Shi, L. D. Chen, G. J. Snyder, *Adv. Mater.* **2014**, *26(23)*, 3974.